

## Supplementary Information

### Dehydration of mildronate dihydrate: a study of structural transformations and kinetics

*Agris Bērziņš, Andris Actiņš*

Faculty of Chemistry, University of Latvia, Rīga, Kr. Valdemāra iela 48, LV-1013, Latvia  
Email: agris.berzins@lu.lv

#### Contents

Analysis of the particle size distribution .....	3
Figure S1. Particle size distribution of different fractions of mildronate dihydrate sample .....	3
Moisture Sorption-Desorption isotherm .....	3
Figure S2. Sorption – desorption isotherm of mildronate.....	4
Study of the mildronate DH dehydration.....	4
Figure S3. PXRD patterns of mildronate dihydrate ( <b>DH</b> ), monohydrate ( <b>MH</b> ) and anhydrous phase ( <b>AP</b> ) .....	4
Figure S4. a) DSC curves of mildronate <b>DH</b> at heating rate 5 °·min <sup>-1</sup> and b) DTA/TG curves of mildronate <b>DH</b> at heating rate 1 °·min <sup>-1</sup> for fractions 1) <40 μm, 2) 40-67 μm, 3) 67-150 μm and 4) 150-350 μm .....	5
Figure S5. DTA/TG curves of mildronate <b>DH</b> at a heating rate of 4 °·min <sup>-1</sup> for fraction >350 μm.....	5
Figure S6. DSC curve of mildronate <b>DH</b> sample for fraction of 67-150 μm (with heating rate 1°·min <sup>-1</sup> ).....	6
Figure S7. Polarized light photomicrographs of the dehydration process of mildronate <b>DH</b> (70-150 μm and 350-700 μm fractions).....	7
Figure S8. Polarized light photomicrographs of the dehydration process of mildronate <b>DH</b> single crystal at 60 – 85 °C and the cross section of the crystal after the heating .....	7
Parameters for calculations in CRYSTAL09.....	7
Crystal structure correction.....	8
Figure S9. Labeling scheme for atoms in crystal structures of <b>DH</b> , <b>MH</b> and <b>AP</b> used for atom position optimization in <i>Gaussian09</i> .....	8
Table S1. Original and final values of mildronate molecule bond lengths, angles and torsion angles affected by crystal structure correction in <i>Gaussian09</i> at the B3LYP/6-31G level and after full structure optimization in <i>CRYSTAL09</i> at the B3LYP-D*/6-31G(d,p) level.....	9
Table S2. Fractional coordinates of all atoms after crystal structure correction in <i>Gaussian09</i> and full structure optimization in <i>CRYSTAL09</i> .....	9
Analysis of the molecule conformation and hydrogen bonding .....	11
Table S3. Torsion angle values of the mildronate molecule in all three crystal structures .....	11

Table S4. The geometric parameters and graph set assignments of hydrogen bonds in mildronate crystalline phases .....	11
Figure S10. Hydrogen bonding motif connecting mildronate molecules (a) in <b>DH</b> and <b>MH</b> and (b) in <b>AP</b> .....	12
Figure S11. Hydrogen bonding motif formed by water molecules in <b>DH</b> (a), and by water and mildronate molecules in <b>MH</b> (b) and <b>DH</b> (c and d) .....	12
Figure S12. Molecular packing and hydrogen bonding network in the crystalline forms of mildronate (hydrogen atoms have been omitted for clarity) .....	12
Analysis of the potential energy surface (PES) scans .....	13
Figure S13. PES scans of mildronate molecule with respect to one torsion angle	13
Figure S14. PES scans of mildronate molecule with respect to two adjacent torsion angles while the rest of the molecule was fixed at conformation observed in <b>DH</b> structure (except bottom right where the rest of the molecule had conformation as in <b>AP</b> structure) .....	15
Figure S15. PES scans of mildronate molecule where two adjacent torsion angles were changed while the rest of the molecule was fixed at conformation observed in <b>AP</b> structure .....	15
Optimization of the molecule conformation of mildronate in <b>DH</b> and <b>AP</b> structures	15
Table S5. Optimized torsion angles of mildronate molecules in <b>DH</b> and <b>AP</b> structures .....	16
Interaction energy of hydrogen bonded molecule pairs .....	16
Table S6. Interaction energy of hydrogen bonded molecule pairs in <b>AP</b> , <b>DHWW</b> and <b>MHWW</b> crystal structures .....	17
Lattice energy of optimized and non-optimized crystal structures .....	17
Table S7. Crystal lattice energy and its components calculated with PIXEL and lattice energy corrected for basis set superposition error, calculated with <i>CRYSTAL09</i> for the original and optimized <b>AP</b> and <b>DHWW</b> structures .....	18
Table S8. The total energy and lattice parameters obtained after the crystal structure optimization in <i>CRYSTAL09</i> for the structures of <b>AP</b> and <b>DHWW</b> .....	19
References .....	20

### Analysis of the particle size distribution

A Mastersizer 2000 (Malvern) laser diffraction instrument was used for particle size analysis. Integration time was 3000 ms. The measurement range was set to 0.020 – 2000  $\mu\text{m}$ , and 59 counting channels were used. For sample dispersion nitrogen with 1.0 bar pressure was used. All measurements were carried out three times and the average value was used.

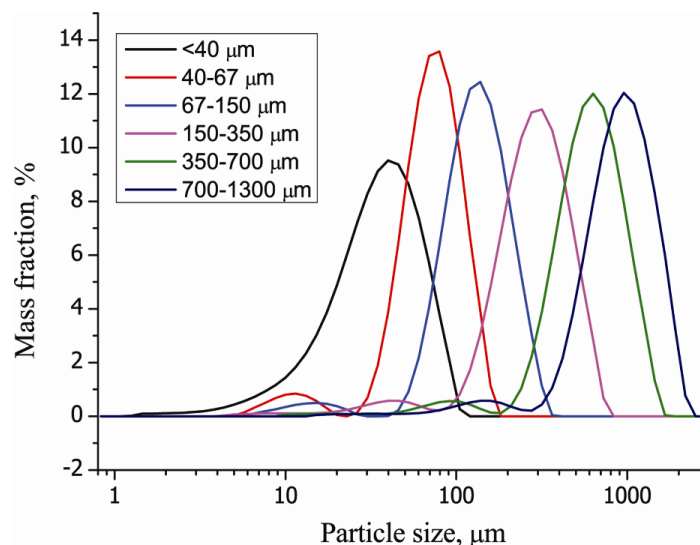


**Figure S1.** Particle size distribution of different fractions of mildronate dihydrate sample

### Moisture Sorption-Desorption isotherm

Mildronate **AP** was used for acquiring a sorption isotherm. **AP** was prepared by heating **DH** at 100 °C temperature. Approximately 0.8 g of sample was weighed in each of ten containers. These containers were placed in humidity chambers where the relative humidity was provided with saturated salt solutions and phosphorus pentoxide. The salts used for this experiment and the corresponding relative humidity values were LiBr (6%), LiCl (11%),  $\text{CH}_3\text{CO}_2\text{K}$  (23%),  $\text{MgCl}_2$  (32%), NaBr (56%), KI (68%), NaCl (75%), KCl (84%),  $\text{K}_2\text{SO}_4$  (97%) and also  $\text{P}_2\text{O}_5$  (~0%)<sup>1</sup>. Humidity chambers were thermostated at 25±1 °C temperature and containers were weighed on analytical balance ( $d=0.1$  mg) until no notable change of mass was observed (except for containers where sample deliquesced). At the end of the experiment, the phase composition of each sample was determined with PXRD. For desorption isotherm, approximately 0.8 g of mildronate **DH** sample stored at 22.5% relative humidity was weighed into containers and inserted in the previously described humidity chambers up to relative the humidity of 32%. The same analytical procedure as described for sorption isotherm was used. Inorganic compounds for relative humidity control were purchased from commercial sources and used without further purification.

From sorption-desorption isotherm of mildronate at 25 °C temperature it was observed that **DH** was stable in the relative humidity interval from 6 to 50% (See Figure S2). Dehydration of **DH** was observed only at 0% relative humidity and **AP** was obtained as the product. By using **AP** as a starting material, it was observed that a

small amount of **DH** formed at 6% relative humidity (~10% of the **AP** transformed into the **DH** over 2 months), while fast transition to **DH** occurred at a higher humidity. By PXRD it was determined that samples contained either **AP** or **DH**. This confirmed<sup>2</sup> that **MH** was not thermodynamically stable at any of the examined conditions. However, continuous monitoring of the phase transition was not done. Thus, it was not possible to exclude the **MH** as a possible transition state in the transformation from **DH** to **AP** or vice versa.

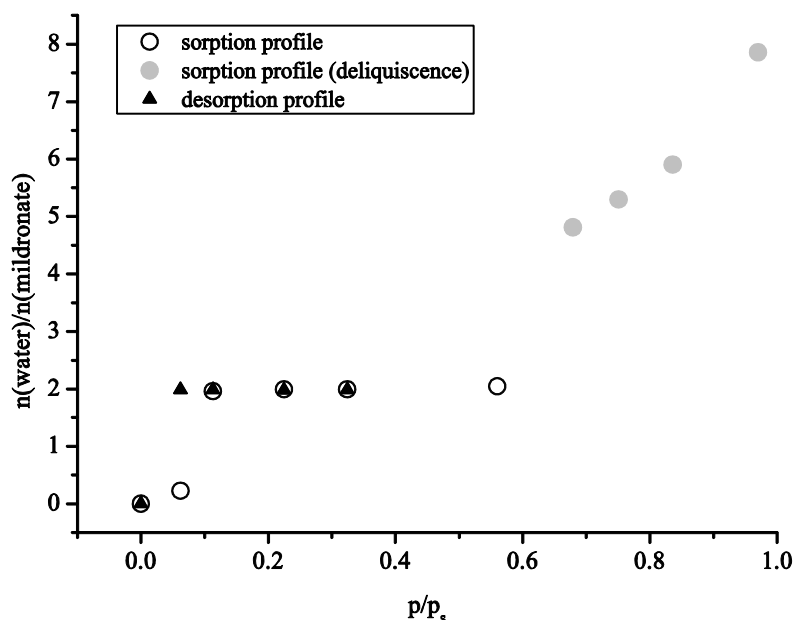


**Figure S2.** Sorption – desorption isotherm of mildronate (water content is given after storing for 2 months)

### Study of the mildronate DH dehydration

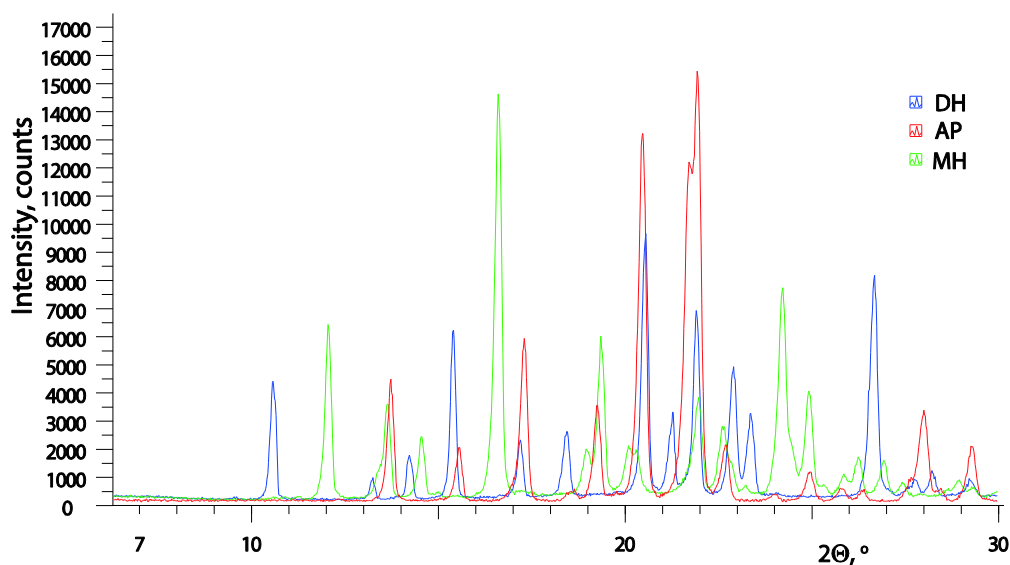


**Figure S3.** PXRD patterns of mildronate dihydrate (**DH**), monohydrate (**MH**) and anhydrous phase (**AP**)

Dehydration of **DH** samples with different particle sizes (the particle size distribution for various fractions is given in Figure S1) was performed during DTA/TG experiments at a heating rate of  $1\text{ }^{\circ}\text{C}\cdot\text{min}^{-1}$  in open pans under nitrogen flow. One endothermic peak appeared with dehydration starting temperature below  $50\text{ }^{\circ}\text{C}$  and the peak thermal effect around  $60\text{--}65\text{ }^{\circ}\text{C}$  (See Figure S4 (b)). For both of these characteristic dehydration temperatures, a significant impact of particle size was observed – dehydration of smaller particles was faster than that of bigger particles at the same heating rate. When analysis of the same samples was performed at a higher heating rate, the dehydration thermal effect was split in two parts (See Figure 3). The second endothermic effect was observed as a relatively sharp peak at  $86\text{--}88\text{ }^{\circ}\text{C}$ . The temperature of this second maximum was not affected by the heating rate or the particle size, and it contributed more at higher heating rates and larger particle sizes. Changing the atmosphere from nitrogen flow to static air increased the dehydration starting temperature and the maximum temperature, while also increasing the contribution from this second maximum. It was also observed that for large particle sizes (above  $350\text{ }\mu\text{m}$ ) after appearance of this second maximum the dehydration rate dropped dramatically, and breaches appeared in the TG line (See Figure S5).

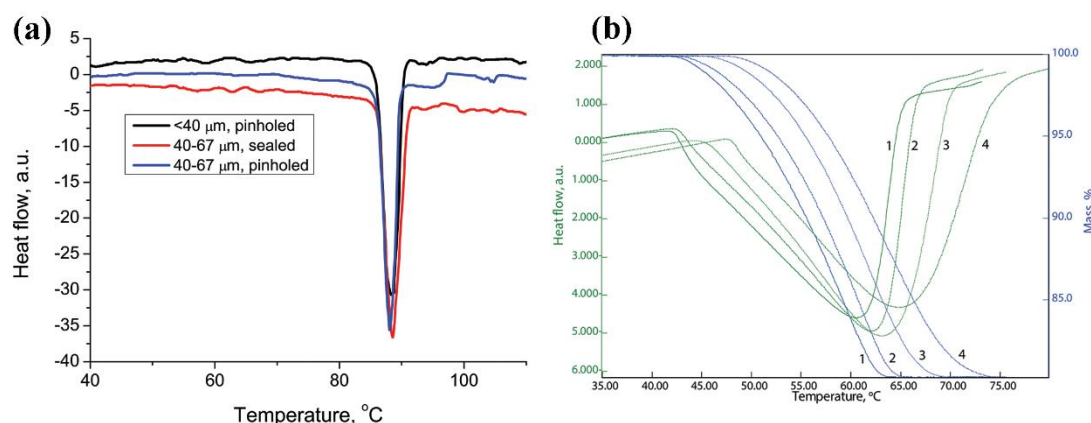


**Figure S4.** a) DSC curves of ildronate **DH** at heating rate  $5\text{ }^{\circ}\text{C}\cdot\text{min}^{-1}$  and b) DTA/TG curves of mildronate **DH** at heating rate  $1\text{ }^{\circ}\text{C}\cdot\text{min}^{-1}$  for fractions 1)  $<40\text{ }\mu\text{m}$ , 2)  $40\text{--}67\text{ }\mu\text{m}$ , 3)  $67\text{--}150\text{ }\mu\text{m}$  and 4)  $150\text{--}350\text{ }\mu\text{m}$ .

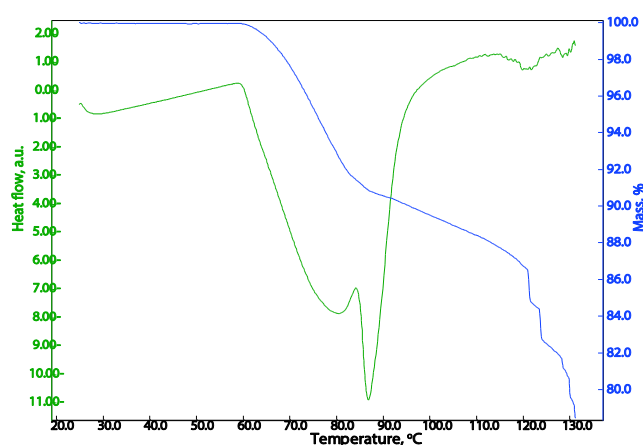


**Figure S5.** DTA/TG curves of mildronate **DH** at a heating rate of  $4\text{ }^{\circ}\text{C}\cdot\text{min}^{-1}$  for fraction  $>350\text{ }\mu\text{m}$

The effect of the atmosphere on the dehydration starting temperature and the temperature of peak dehydration rate could be easily explained by the fact that dehydration process was affected by the moisture content in the atmosphere. By providing a dry nitrogen flow, water was effectively removed from the sample, thus enhancing the dehydration rate. The effect of heating rate could be associated with the total heating time, thus a higher conversion degree for given temperature was obtained with slower heating rates. The observation that smaller particles dehydrated faster can be associated with the larger surface to mass ratio and it is known that dehydration reactions typically start on the surface where the dehydration is enhanced<sup>3</sup>.

It was determined that the only factor affecting the dehydration peak position and shape in the DSC experiments was the heating rate. When the heating rate was  $1\text{ }^{\circ}\text{C}\cdot\text{min}^{-1}$ , dehydration starting temperature decreased to the same value as was observed in the VT-PXRD experiment, although a sharp peak at  $87\text{ }^{\circ}\text{C}$  was still observed (See Figure S6).

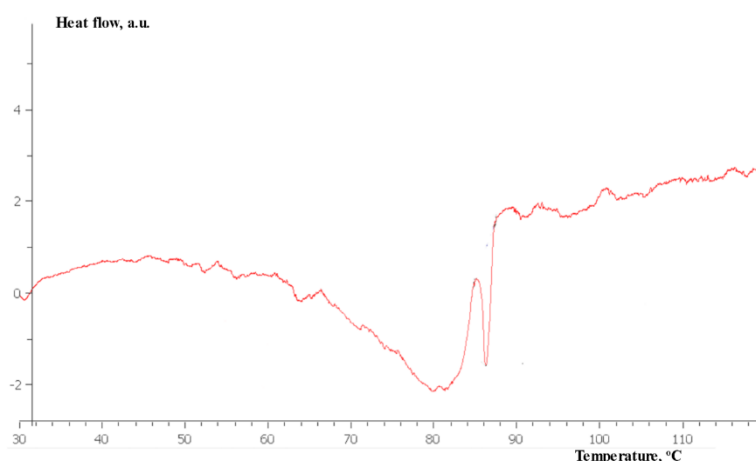


**Figure S6.** DSC curve of mildronate **DH** sample for fraction of 67-150  $\mu\text{m}$  (with heating rate  $1\text{ }^{\circ}\text{C}\cdot\text{min}^{-1}$ )

In order to get more insight into the processes occurring during the dehydration of **DH** and to explain observations from thermal analysis, dehydration of 67-150  $\mu\text{m}$  and 350-700  $\mu\text{m}$  **DH** fractions was analysed with hot stage polarized light microscopy. When particles from the 67-150  $\mu\text{m}$  fraction were heated at the rate of  $8\text{ }^{\circ}\text{C}\cdot\text{min}^{-1}$ , sample darkening was observed at  $70\text{ }^{\circ}\text{C}$  temperature and no further changes were observed until the temperature of  $140\text{ }^{\circ}\text{C}$  was reached (see Figure S7). When particles from the 350-700  $\mu\text{m}$  fraction were analysed, the sample darkened at  $72\text{ }^{\circ}\text{C}$ . When the temperature reached almost  $90\text{ }^{\circ}\text{C}$ , emanation of liquid water was observed from most of the crystals, and this process continued upon further heating of the sample. Bubbling of evolved water was observed above  $100\text{ }^{\circ}\text{C}$ , and the bubbling intensified upon further increasing of the temperature. In some of the experiments within the temperature interval of  $115 - 130\text{ }^{\circ}\text{C}$  some of the crystals from the 350-700  $\mu\text{m}$  fraction even exploded.

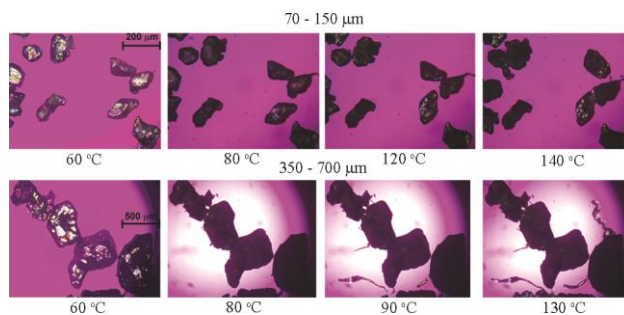


**Figure S7.** Polarized light photomicrographs of the dehydration process of mildronate DH (70-150  $\mu\text{m}$  and 350-700  $\mu\text{m}$  fractions).

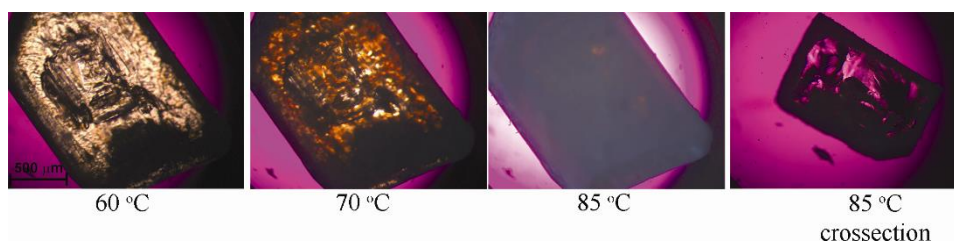


**Figure S8.** Polarized light photomicrographs of the dehydration process of mildronate DH single crystal at 60 – 85  $^{\circ}\text{C}$  and the cross section of the crystal after the heating.

Thus, above the peritectic temperature mildronate water solution formed by abruptly slowing down the dehydration process, as observed in DTA/TG scans. Crystal explosion most probably happened due to the fact that the newly formed AP surrounded the crystal, which temporarily blocked the release of water. After the peritectic temperature was reached, liquid water was released in the interior of the particle. Water was not able to escape the particle, and increasing the temperature led to a pressure increase, followed by disruption of the particle. This observation agrees with the appearance of branches in DTA/TG curves for larger particle sizes.

### Parameters for calculations in *CRYSTAL09*

The level of accuracy in evaluating the Coulomb and exchange series was controlled by five thresholds<sup>4</sup>, for which values  $10^{-8}$ ,  $10^{-7}$ ,  $10^{-7}$ ,  $10^{-7}$  and  $10^{-24}$  were used as suggested in the literature<sup>5</sup>, in order to avoid numerical instabilities in computing the exact exchange contributions. For numerical integration of the density (75, 974)p, an extra-large grid was adopted<sup>4</sup>. The irreducible Brillouin zone was sampled using 170 k-points (the shrinking factor<sup>4</sup> of the reciprocal space net was set to 8). Levshift function with level shift of 1 hartree without locking was used in order to reach the convergence in energy. Full crystal structure optimization was done with analytical gradients for the unit cell. For optimization procedure, the space group symmetry of the original crystal structures was retained. Convergence criteria for geometry optimization were as follows: maximum energy gradient/component = 0.00045, RMS energy gradient/component = 0.0003, maximum displacement/component = 0.0018, RMS displacement/component = 0.0012, threshold for energy change =  $0.1 \cdot 10^{-6}$ , all in a.u.



## Crystal structure correction

The crystal structures of **AP** and **MH** had previously been determined from PXRD data, thus only positions of non-hydrogen atoms were reported<sup>6</sup>. Moreover, the reported bond distances of carboxyl group oxygen atoms were not optimized but left as in non-conjugated systems<sup>6</sup>. The structural information for **AP** and **MH** was taken from the literature<sup>6</sup> and improvements in the following order were applied: 1) hydrogen atoms were added, 2) molecular cluster consisting of a central molecule surrounded by 12 closest neighbour molecules was prepared. Positions of central molecule's carboxyl group oxygen atoms O1 and O2, hydrogen atom bounded to nitrogen H1, hydrogen atoms of water molecules H15, H16 (in **MH** and **DH**), H17 and H18 (in **DH**), to central molecule's N-H intermolecular hydrogen bonded oxygen (O1' in **AP** and O2' in **MH**), the hydrogen bound to central molecule's carboxyl group (H1'') and hydrogen atoms of water molecule H15'' and H16'' (in **MH**) (See Fig. S2) were optimized at the B3LYP/6-31G level in *Gaussian09*<sup>7</sup>. It should be remarked that the dihedral angle  $\tau_1$  was altered after this operation. 3) Positions of all hydrogen atoms of the central molecule were optimized at the B3LYP/6-31G level in *Gaussian09*<sup>7</sup>. For further calculations, the corrected structure of **AP** and **MH** was used. Corrected **DH** structure was used only for extraction of mildronate molecules to calculate the intramolecular energy.

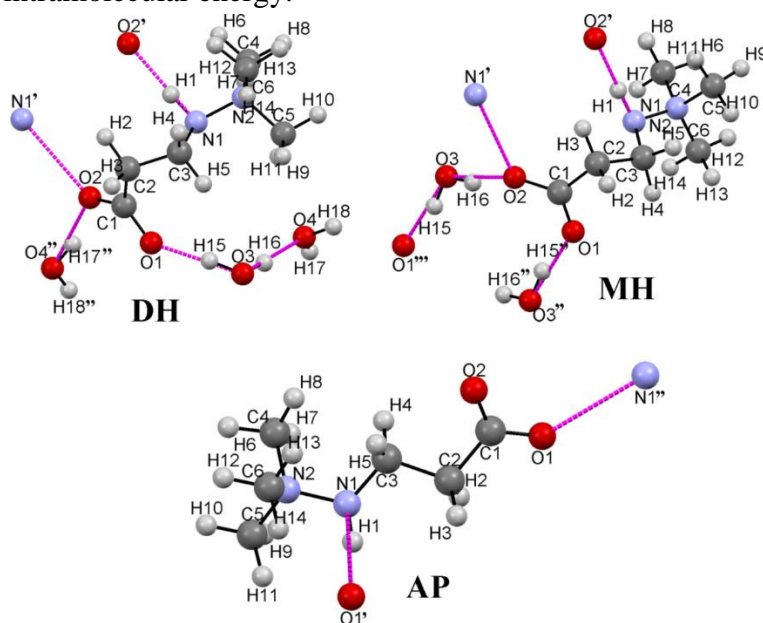


**Figure S9.** Labeling scheme for atoms in crystal structures of **DH**, **MH** and **AP** used for atom position optimization in *Gaussian09*

The values of bond distances, angles, and dihedral angles, which were changed during the crystal structure correction in *Gaussian09* in all three structures, are given in Table 1S. All atom positions in fractional coordinates after optimization are given in Table 2S. By comparing the obtained data with the results from crystal structure optimization in *CRYSTAL09*, it can be seen that there were only minor differences, meaning that the procedure performed in *Gaussian09* was reliable and the corrected crystal structures were suitable for further use.



**Table S1.** Original and final values of mildronate molecule bond lengths, angles and torsion angles affected by crystal structure correction in *Gaussian09* at the B3LYP/6-31G level and after full structure optimization in *CRYSTAL09* at the B3LYP-D\*/6-31G(d,p) level

Parameter	AP			MH		DH		
	Original <sup>6</sup>	Optimized <sup>a</sup>	Optimized <sup>b</sup>	Original <sup>6</sup>	Optimized <sup>a</sup>	Original <sup>8</sup>	Optimized <sup>a</sup>	Optimized <sup>b</sup>
d(O1-C1)	1.21	1.275	1.270	1.21	1.279	1.257	1.276	1.258
d(O2-C1)	1.36	1.255	1.258	1.36	1.307	1.267	1.307	1.275
d(N1-H14)	-	1.013	1.035	-	1.010	0.919	1.045	1.032
Angle(O1-C1-O2)	1.20	124.7	125.65	120.0	123.1	123.7	123.1	123.3
Angle(O1-C1-C2)	1.20	119.9	115.64	120.0	118.2	118.5	120.4	119.2
Angle(C3-N1-H1)	-	111.1	109.21	-	111.6	108.9	109.4	108.1
Torsion(O1-C1-C2-C3)	175.1	-156.2	-179.6	45.3	47.8	51.4	49.0	52.8
Torsion(C2-C3-N1-H1)	-	55.3	63.14	-	48.0	57.0	52.2	52.3

<sup>a</sup> – optimization of central molecule in molecule cluster in *Gaussian09* at the B3LYP/6-31G level

<sup>b</sup> – full crystal structure optimization in *CRYSTAL09* at the B3LYP-D\*/6-31G(d,p) level

**Table S2.** Fractional coordinates of all atoms after crystal structure correction in *Gaussian09* and full structure optimization in *CRYSTAL09*

Code		<i>Gaussian09</i>								<i>CRYSTAL09</i>					
Form		AP			MH			DH		AP			DH		
O1	0.7805	1.1208	0.8543	0.7081	0.2152	0.6783	0.4451	0.1202	0.6766	0.7576	1.1022	0.8876	0.4562	0.1272	-0.3267
C1	0.7252	1.0653	0.7254	0.6518	0.3032	0.5596	0.3205	0.0811	0.5923	0.7214	1.0680	0.7349	0.3237	0.0845	-0.4084
O2	0.6117	1.0986	0.6356	0.7478	0.4510	0.3868	0.2144	0.1498	0.5172	0.6201	1.1154	0.6394	0.2020	0.1509	-0.4803
C2	0.7986	0.9477	0.6916	0.4686	0.2253	0.6141	0.3011	-0.0520	0.5702	0.8133	0.9603	0.6635	0.3096	-0.0537	-0.4255
H2	0.9200	0.9523	0.7236	0.4548	0.1026	0.5797	0.1738	-0.0681	0.5010	0.9374	0.9831	0.6658	0.1827	-0.0753	-0.4975
H3	0.7494	0.8823	0.7738	0.4306	0.3223	0.5180	0.4360	-0.0805	0.5480	0.7984	0.8867	0.7561	0.4503	-0.0830	-0.4432
C3	0.7743	0.9158	0.5035	0.3549	0.1695	0.8540	0.2797	-0.1270	0.6653	0.7693	0.9207	0.4791	0.2899	-0.1273	-0.3265
H5	0.8168	0.9878	0.4295	0.2309	0.0770	0.9000	0.3941	-0.1022	0.7380	0.8002	0.9910	0.3867	0.4067	-0.0990	-0.2525
H4	0.6530	0.9068	0.4739	0.4104	0.0935	0.9434	0.2993	-0.2203	0.6478	0.6433	0.9068	0.4698	0.3131	-0.2236	-0.3419

N1	0.8651	0.8103	0.4644	0.3399	0.3331	0.8985	0.0795	-0.1003	0.6808	0.8630	0.8146	0.4376	0.0863	-0.1014	-0.3129
H1	0.8388	0.7432	0.5433	0.3113	0.4208	0.7920	-0.0293	-0.1124	0.6081	0.8331	0.7471	0.5238	-0.0216	-0.1165	-0.3871
N2	0.8415	0.7676	0.2946	0.2170	0.2947	1.1123	0.0215	-0.1773	0.7602	0.8322	0.7605	0.2657	0.0246	-0.1808	-0.2347
C5	0.9502	0.6713	0.2645	0.0460	0.1992	1.1544	0.1400	-0.1432	0.8706	0.9457	0.6584	0.2550	0.1439	-0.1466	-0.1198
C4	0.8684	0.8616	0.1701	0.2160	0.4676	1.1370	-0.1965	-0.1520	0.7471	0.6667	0.7160	0.2461	-0.1986	-0.1541	-0.2519
C6	0.6832	0.7231	0.2708	0.2602	0.1838	1.2696	0.0452	-0.3075	0.7430	0.8691	0.8458	0.1191	0.0501	-0.3156	-0.2522
H9	1.0646	0.7067	0.2763	-0.0478	0.2010	1.3020	0.2934	-0.1736	0.8836	1.0619	0.6969	0.2640	0.1360	-0.0483	-0.1106
H10	0.9316	0.6364	0.1383	0.0331	0.0581	1.1748	0.0739	-0.1856	0.9288	0.9301	0.6136	0.1301	0.3024	-0.1751	-0.1054
H11	0.9341	0.6047	0.3599	0.0242	0.2693	1.0214	0.1364	-0.0477	0.8788	0.9219	0.5999	0.3659	0.0758	-0.1936	-0.0634
H12	0.6699	0.6893	0.1430	0.1719	0.1744	1.4277	-0.2774	-0.1797	0.6664	0.5836	0.7885	0.2655	-0.2158	-0.0573	-0.2382
H13	0.5999	0.7918	0.2871	0.2533	0.0493	1.2670	-0.2150	-0.0575	0.7565	0.6471	0.6477	0.3450	-0.2789	-0.1784	-0.3360
H14	0.6650	0.6551	0.3631	0.3890	0.2553	1.2306	-0.2475	-0.2034	0.8062	0.6555	0.6807	0.1140	-0.2555	-0.2097	-0.1962
H6	0.8658	0.8220	0.0454	0.1202	0.4406	1.2975	-0.0330	-0.3291	0.6602	0.9870	0.8802	0.1356	0.2126	-0.3374	-0.2272
H7	0.9812	0.8979	0.1929	0.3404	0.5367	1.1131	-0.0231	-0.3549	0.7977	0.7832	0.9171	0.1166	-0.0218	-0.3371	-0.3381
H8	0.7794	0.9267	0.1756	0.1862	0.5515	1.0191	0.2036	-0.3291	0.7620	0.8638	0.7941	-0.0014	-0.0268	-0.3658	-0.2016
O3				0.9950	0.7438	0.3183	0.5994	0.0778	0.8884				-0.3996	0.0736	-0.1124
H15				1.1007	0.7378	0.3308	0.5402	0.0876	0.8098				-0.4575	0.0837	-0.1920
H16				0.9141	0.6252	0.3580	0.4964	0.1029	0.9270				0.4896	0.0980	-0.0806
O4							0.3112	0.1251	0.9945				0.3017	0.1222	-0.0181
H17							0.2773	0.2048	1.0179				0.2762	0.2031	0.0095
H18							0.3248	0.0573	1.0463				0.3276	0.0612	0.0413

<sup>a</sup> – optimization of central molecule in molecule cluster in Gaussian09 at the B3LYP/6-31G level, lattice parameters unchanged

<sup>b</sup> – full crystal structure optimization in CRYSTAL09 at the B3LYP-D\*/6-31G(d,p) level, lattice parameters given in Table 1

## Analysis of the molecule conformation and hydrogen bonding

It is already stated that conformation of mildronate molecule is almost the same for the **DH** and **MH** (see Table S3). Torsion angles O1-C1-C2-C3 ( $\tau_1$ ) and C1-C2-C3-N1 ( $\tau_2$ ) in **AP** are significantly different than those in **DH** and **MH**. Hydrogen bond geometry of **DH**, **MH** and **AP** is presented in Table S4. Geometry of hydrogen bonds in **MH** and **AP** structures was determined after structure correction at the B3LYP level. Analysis of hydrogen bonding motifs in crystal structure showed that inversion related mildronate moieties in crystal structures of **DH** and **MH** form N1-H1 $\cdots$ O2 hydrogen bonded dimers with graph set  $R_2^2(12)$  (See Figure S10 (a)). Additionally, mildronate carboxyl groups and water molecules in **MH** form O-H $\cdots$ O hydrogen bonds with second order graph set  $R_4^4(12)$  (See Fig. S11). In crystal structure of **DH** four water molecules form hydrogen bonded  $R_4^4(8)$  motifs (See Fig. S11). Water molecules are connected to mildronate molecules by infinite  $C_3^3(8)$  and  $C_3^4(12)$  chains (See Fig. S11). In **AP** crystal structure mildronate molecules form N1-H1 $\cdots$ O1 hydrogen bonded chains designated by C(6) graph set (See Figure S10 (b)).

**Table S3.** Torsion angle values of the mildronate molecule in all three crystal structures

Angle	O1-C1-C2-C3	C1-C2-C3-N1	C2-C3-N1-N2	C3-N1-N2-C4
	$\tau_1, ^\circ$	$\tau_2, ^\circ$	$\tau_3, ^\circ$	$\tau_4, ^\circ$
<b>DH</b> <sup>8</sup>	51.4	69.4	172.1	-169.2
<b>MH</b> <sup>6</sup>	45.3	74.6	171.5	179.2
<b>AP</b> <sup>6</sup>	175.1	171.6	175.5	54.0
<b>AP</b> <sub>corr</sub> <sup>a</sup>	-156.2	171.6	175.5	54.0

<sup>a</sup> – optimization of central molecule in molecule cluster in Gaussian09 at the B3LYP/6-31G level

**Table S4.** The geometric parameters and graph set assignments of hydrogen bonds in mildronate crystalline phases

Hydrogen bond	Symmetry	D-H, Å	H⋯A, Å	D-A, Å	∠DHA, °	Graph set notation
<b>DH</b>						
N1—H1⋯O2	-x, -y, 1-z	0.919	2.004	2.920	175.5	$R_2^2(12)$
O4—H18⋯ O3	1-x,-y,2-z	0.988	1.775	2.728	161.1	} $R_4^4(8)$
O3—H16⋯ O4	x,y,z	1.171	1.594	2.760	173.5	
O4—H17⋯ O2	x,1/2-y,1/2+z	0.777	0.955	2.714	165.4	
O3—H15⋯ O1	x,y,z	0.786	1.941	2.719	170.3	
<b>MH</b>						
N1—H1⋯ O2	1-x,1-y,1-z	1.040	1.742	2.779	1774.4	$R_2^2(12)$
O3—H16⋯ O2	x,y,z	0.991	1.782	2.748	164.1	} $R_4^4(12)$
O3—H15⋯ O1	2-x,1-y,1-z	1.002	1.675	2.657	165.6	
<b>AP</b>						
N1—H1⋯ O1	1,5-x,1/2+y,1.5-z	1.013	1.925	2.894	159.0	$C(6)$

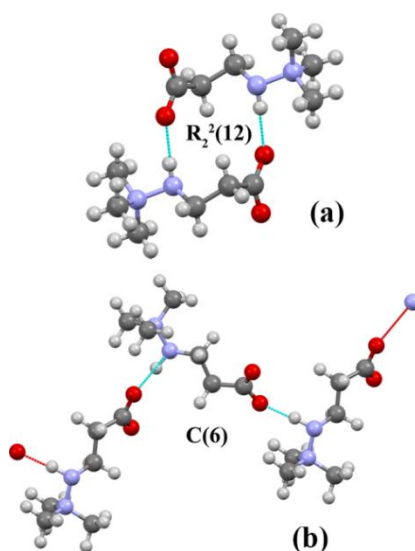


**Figure S10.** Hydrogen bonding motif connecting mildronate molecules (a) in **DH** and **MH** and (b) in **AP**

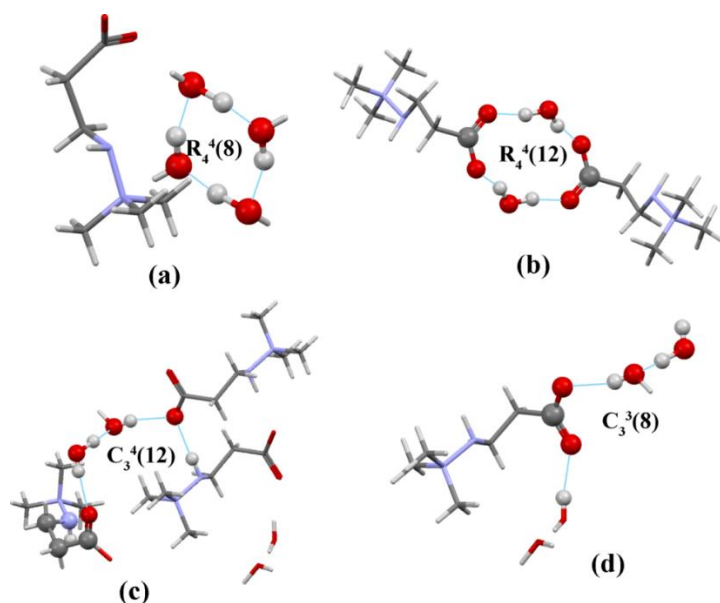


**Figure S11.** Hydrogen bonding motif formed by water molecules in **DH** (a), and by water and mildronate molecules in **MH** (b) and **DH** (c and d)

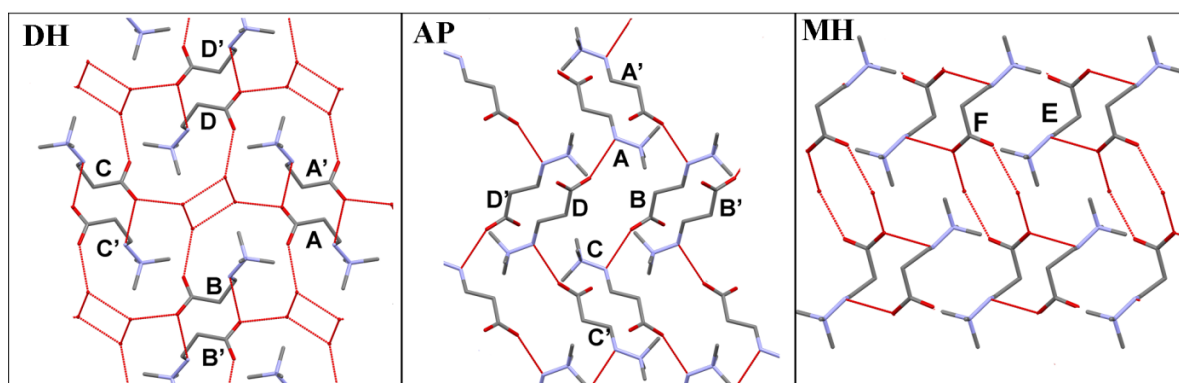


**Figure S12.** Molecular packing and hydrogen bonding network in the crystalline forms of mildronate (hydrogen atoms have been omitted for clarity).

### Analysis of the potential energy surface (PES) scans

In order to examine the potential energy surface (PES) of observed conformations with respect to other available conformations all four torsion angles were scanned at the MP2/6-31G(d,p) level with step size of  $10^\circ$  while conformation for the rest of the molecule was maintained as observed whether in **DH** or **AP** structure. For this analysis mildronate molecule was extracted from nonoptimized **DH** structure with atom coordinates as in the literature and from **AP** structure corrected at the B3LYP/6-31G level. PES scans with marked torsion angles as observed in experimental structures are presented in Figure S13. It can be seen that the form of PES scans with respect to the same torsion angle slightly depends on the conformation of the rest of the molecule although the positions of minimums and maximums are generally at the same angles.

Minimums in the PES scan with respect to torsion angle  $\tau_1$  (Figure S13) can be associated with C3-H $\cdots$ O1 (in experimental **DH** structure) and C3-H $\cdots$ O2 (in experimental **AP** structure) interaction while maximums are associated with intramolecular interactions N1 $\cdots$ O1 and N1 $\cdots$ O2. In the scan with respect to torsion angle  $\tau_2$  global minimum is observed when intramolecular hydrogen bonding N1-H $\cdots$ O1 (in **DH**) and N1-H $\cdots$ O2 (in **AP**) is present, maximum at  $\tau_2 = 0$  is related to eclipsed conformation where N1 $\cdots$ O1(8) interaction is observed but local minimums are due to C3-H $\cdots$ O1 (in **DH**) and C3-H $\cdots$ O2 (in **AP**) intramolecular interaction. Energy difference between global minimum and global maximum is higher in **AP** structure due to shorter distances in observed interactions. Experimental structures correspond to different local energy minimums. Energy maximums in  $\tau_3$  scan is associated with close C1-H $\cdots$ H-C4 and C1-H $\cdots$ H-C6 interaction in **AP** and with methyl group close interaction with carboxyl group and with close C1-H $\cdots$ H-C5 and C1-H $\cdots$ H-C6 interaction in **DH**. Although it seems that from  $\tau_3 = 100$  to  $-100^\circ$  there is a plateau with the same energy, closer look reveals that **AP** is located in global energy minimum while **DH** in local minimum. Energy scan of  $\tau_4$  corresponds to conformational energy diagram for rotation around single bond with observed crystal structures situated in global energy minimums.

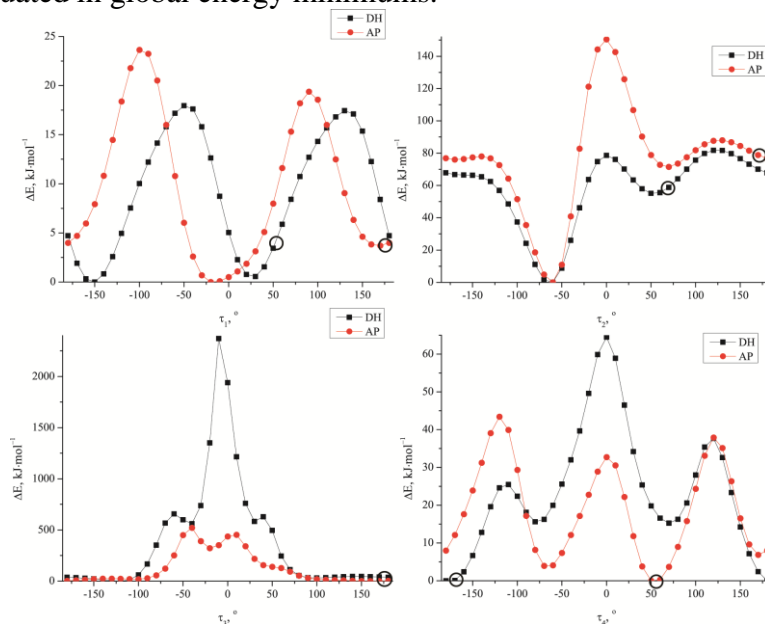


**Figure S13.** PES scans of mildronate molecule with respect to one torsion angle (the rest of the molecule was fixed at conformation observed in **DH** or **AP** structure)

By analysing the PES graphs with respect to one dihedral angle, it was calculated that the energy barrier necessary for conformation changes during the transition from **DH** to **AP** was 15 kJ·mol<sup>-1</sup> for changing  $\tau_1$ , 10-25 kJ·mol<sup>-1</sup> for changing  $\tau_2$ , and 30-40 kJ·mol<sup>-1</sup> for changing  $\tau_4$ . From these results it can be seen that the activation energy necessary for conformation changes was slightly lower than typical energy barriers in phase transitions.

To more realistically evaluate the activation energy necessary for transformation of molecular conformation, PES graphs with respect to two dihedral angles were created as well. In this transition from **DH** to **AP**, where the dihedral angles  $\tau_3$  and  $\tau_4$  did not change, a pathway where simultaneous changes dihedral angles  $\tau_1$  -  $\tau_2$  could be important.

PES with respect to two adjacent torsion angle change of all three adjacent torsion angle combinations were performed at the B3LYP/6-31G level with step size 15° for each dihedral angle and it was observed that PES for torsion angles  $\tau_1$ - $\tau_2$  and  $\tau_2$ - $\tau_3$  are basically the same for **DH** and **AP** conformations while PES scan for torsion angle  $\tau_3$ - $\tau_4$  changes is different for both structures. All three PES scans for **DH** structure and  $\tau_3$ - $\tau_4$  scan for **AP** is showed in Figure S14 but the rest two scans for **AP** structure are shown in Figure S15. Energy minimums observed in PES scan with respect to  $\tau_1$ - $\tau_2$  1 and 1' and minimum 2 in scan with respect to  $\tau_2$ - $\tau_3$  corresponds to intramolecular hydrogen bond N1-H··O1(O2), but minimum 3 corresponds to weak intramolecular hydrogen bond C5-H··O1 in **DH** and C3-H··O2 in **AP**. Energy maximum in PES scan with respect to  $\tau_1$ - $\tau_2$  corresponds to N1··O1 and N1··O2 interaction. In scan with respect to  $\tau_1$ - $\tau_2$  **DH** and **AP** structures are located in local energy minimums and changes from one conformation to second one is associated with energy barrier 20 kJ·mol<sup>-1</sup>. In PES scan with respect to  $\tau_3$ - $\tau_4$  conformation as in **AP** structure corresponds to global minimum without specific interaction. However, in **DH** global minimum 4 corresponds to C5-H··O1 interaction. Energy maximums in PES scans with respect to  $\tau_2$ - $\tau_3$  and  $\tau_3$ - $\tau_4$  correspond to unrealistic overlapping of atoms or unrealistically short intramolecular distances explaining huge energy difference comparing with observed conformations.

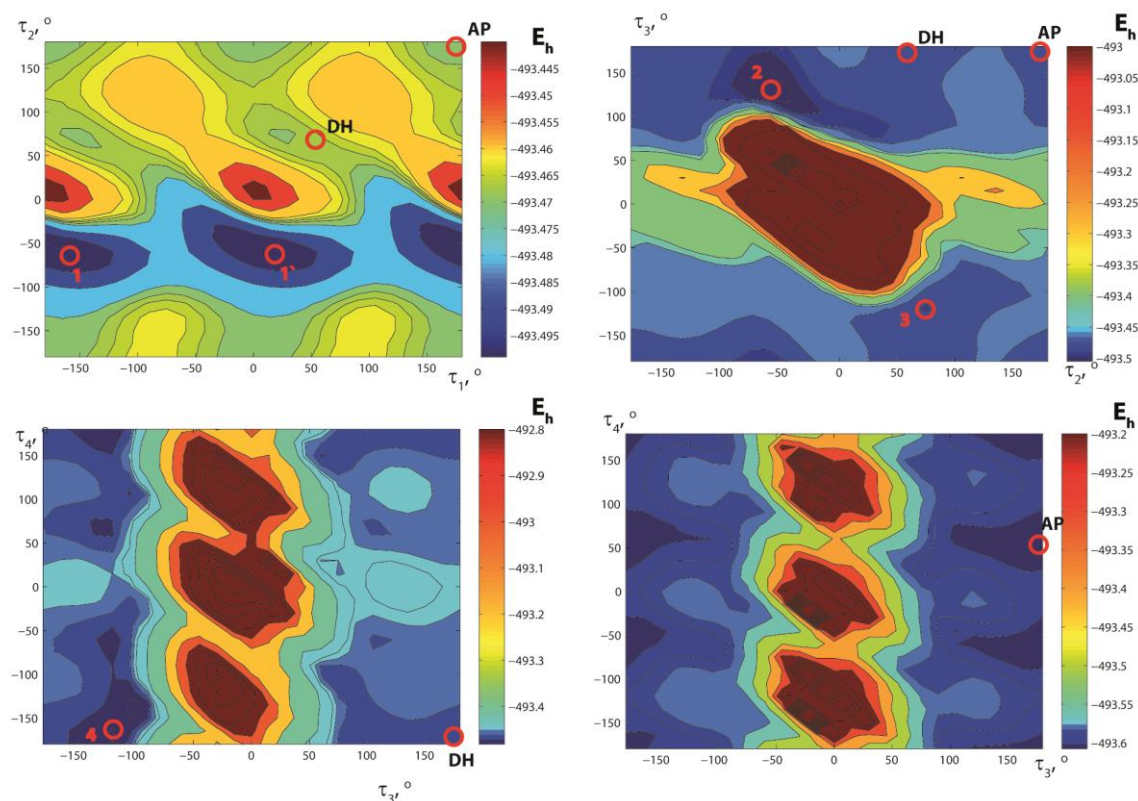


**Figure S14.** PES scans of mildronate molecule with respect to two adjacent torsion angles while the rest of the molecule was fixed at conformation observed in **DH** structure (except bottom right where the rest of the molecule had conformation as in **AP** structure)

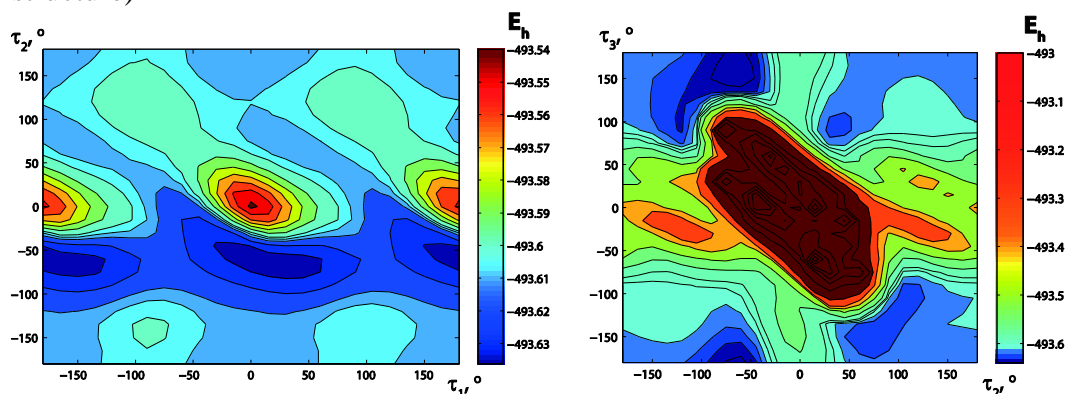


**Figure S15.** PES scans of mildronate molecule where two adjacent torsion angles were changed while the rest of the molecule was fixed at conformation observed in **AP** structure

### Optimization of the molecule conformation of mildronate in **DH** and **AP** structures

Torsion angle optimization of mildronate molecule surrounded by 12 closest molecules was performed in *Gaussian09* at the B3LYP/6-31G level for both **DH** and **AP** structures. This procedure was repeated several times by updating the conformation of surrounding molecules with the goal to prove that observed conformation is the most stable in the experimental crystal structures. Full crystal



structure optimization of both **DH** and **AP** was performed in *CRYSTAL09*. Results are shown in Table S5.

**Table S5.** Optimized torsion angles of mildronate molecules in **DH** and **AP** structures

Angle	$\tau_1, ^\circ$	$\tau_2, ^\circ$	$\tau_3, ^\circ$	$\tau_4, ^\circ$
<b>DH</b>				
Original <sup>8</sup>	51.4	69.4	172.1	-169.2
HF/STO3G 3rd iteration	58.7	71.5	172.5	-170.6
HF/6-31G 1st iteration	55.0	66.0	176.4	-165.5
HF/6-31G 2nd iteration	53.9	67.7	175.2	-165.0
B3LYP-D* <i>CRYSTAL09</i>	52.8	68.9	169.3	-169.0
<b>AP</b>				
Original <sup>6,a</sup>	175.1	171.6	175.5	54.0
HF/STO3G 3rd iteration	-158.9	-177.7	177.1	55.4
HF/6-31G 1st iteration	-158.4	176.6	172.0	51.7
HF/6-31G 2nd iteration	-162.3	173.3	175.0	53.9
B3LYP-D* <i>CRYSTAL09</i>	-179.6	-177.4	177.9	61.6

<sup>a</sup> – Torsion angle values from the literature<sup>6</sup> were used while all other parameters were used from crystal structure corrected in *Gaussian09* at the B3LYP level.

Torsion angles in *Gaussian09* calculations have been changed by less than 5 ° with one exception of  $\tau_1$  of **AP** structure which has been changed by more than 20 ° while after calculations in *CRYSTAL09* changes up to 10° for **AP** structure were observed. It should be remembered that similar torsion angle  $\tau_1$  value for **AP** structure was obtained also when full oxygen and hydrogen atom position optimization in the molecule cluster was performed during structure correction in *Gaussian09*. Such a big change can be explained by previous optimization of oxygen atom bond distance and angle in such a way changing molecular environment. Differences between results from both calculation methods are associated with more accurate periodic boundary approach in *CRYSTAL09* and different calculation levels used. Also it can be seen that after full optimization in *CRYSTAL09* only minor changes in conformation of mildronate molecules in **DH** structure are introduced thus confirming that the **AP** crystal structure probably is less accurate due to the determination from the PXRD data. Thus it can be seen that molecule conformation observed in crystal structures correspond to energy minimum in crystalline environment.

### Interaction energy of hydrogen bonded molecule pairs

To compare the intermolecular energy of the **AP** and **DHWW** structures, at first the hydrogen bonding energy of mildronate molecules in the crystal structure was calculated. The interaction energy between hydrogen bonded molecules is shown in Table S6. However, it should be noted that in **DHWW** two hydrogen bonds formed between two molecules while in **AP** each molecule formed two hydrogen bonds, each with a different molecule. Thus, the interaction energy given in Table S6 corresponded to two hydrogen-bonds in the **DHWW** structure, but only one hydrogen bond in the **AP** structure, so the energy value obtained for **DHWW** was related to one hydrogen bond. It can be seen that the total interaction energy of two molecules was more favourable in the **DHWW** structure. By analysing the contribution from different types of interactions, it was concluded that the Coulomb energy dominated

in both of these dimers, which was already expected for a molecule with highly polar groups, especially because mildronate molecule is a zwitterion. It can also be evaluated that all four energy types contributed similarly to the total energy of dimers from both structures and the main differences in the total energy resulted from more negative Coulomb energy in **DHWW** structure and small differences of other energy types.

**Table S6.** Interaction energy of hydrogen bonded molecule pairs in **AP**, **DHWW** and **MHWW** crystal structures.

Phase	Symmetry operation	$d_r$ , Å <sup>a</sup>	$E_{col}$ , kJ·mol <sup>-1</sup>	$E_{pol}$ , kJ·mol <sup>-1</sup>	$E_{disp}$ , kJ·mol <sup>-1</sup>	$E_{rep}$ , kJ·mol <sup>-1</sup>	$E_{tot}$ , kJ·mol <sup>-1</sup>
<b>AP</b>	1,5-x, -1/2+y, 1,5-z	7.09	-111.0	-42.7	-18.2	49.5	-122.4
<b>DHWW</b>	-x, -y, 1-z	4.96	-238.4	-80.0	-36.6	89.5	-265.5
	Per 1 hydrogen bond:		-119.2	-40.0	-18.3	44.75	-132.75
<b>MHWW</b>	1-x, 1-y, 1-z	4.91	-273.3	-98.0	-40.1	143.8	-267.7
	Per 1 hydrogen bond:		-136.7	-49.0	-20.1	71.9	-133.9

<sup>a</sup> -  $d_r$  is distance between mass centers of the molecules, Å

Additionally, interaction energy of mildronate molecule dimer in **MH** structure was calculated and given in Table S6. By comparing the interaction energy of mildronate dimers in **DH** and **MH** structures, it can be seen that the total interaction energy is the same, although components slightly differed – Coulomb and polarization energy terms were more negative for **MH** and the repulsion energy term was more positive. This result could be associated with the fact that molecules in hydrogen bonded pairs in the **MH** structure were situated closer to each other.

### Energy of optimized and non-optimized crystal structures

The obtained lattice energy for both structures is given in Table S7. As expected for non-optimized crystal structures, by both calculation methods it was determined that the lattice energy of **AP** was lower than that of **DHWW** by 33.0 kJ·mol<sup>-1</sup> (from *PIXEL*) and 20.4 kJ·mol<sup>-1</sup> (from *CRYSTAL09*), due to the large empty channels in the **DHWW** structure. By comparing the contribution from lattice energy components calculated with *PIXEL*, it can be seen that the Coulomb, polarization and dispersion energy was more negative in **AP** structure, while repulsion energy was lower in the **DHWW** structure. This could be explained by the fact that molecules in **AP** were packed more compactly than in non-optimized **DHWW** structure.

**Table S7.** Crystal lattice energy and its components calculated with *PIXEL* and lattice energy corrected for basis set superposition error, calculated with *CRYSTAL09* for the original (SP) and optimized (OP) **AP** and **DHWW** structures.

	$E_{\text{Coul}}, \text{kJ}\cdot\text{mol}^{-1}$	$E_{\text{Pol}}, \text{kJ}\cdot\text{mol}^{-1}$	$E_{\text{Disp}}, \text{kJ}\cdot\text{mol}^{-1}$	$E_{\text{Rep}}, \text{kJ}\cdot\text{mol}^{-1}$	$E_{\text{Tot}}, \text{kJ}\cdot\text{mol}^{-1}$
<b>AP</b>					
PIXEL <sub>SP</sub>	-278.9	-79.8	-110.5	160.7	-308.4
CRYSTAL09 <sub>SP</sub>					-330.4
CRYSTAL09 <sub>OP</sub>					-334.9
<b>DHWW</b>					
PIXEL <sub>SP</sub>	-222.1	-58.4	-73.5	78.6	-275.4
CRYSTAL09 <sub>SP</sub>					-309.5
CRYSTAL09 <sub>OP</sub>					-320.9

In order to allow for possible reorganization in the **DHWW** structure after the water loss, crystal structure optimization was carried out with the *ab initio* code *CRYSTAL09*. Moreover, optimization was performed also for **AP**, to ensure that both structures are compared at the same conditions, because optimization (temperature-less relaxation) of the structure determined at room temperature led to cell shrinkage<sup>9</sup>).

After the optimization reduction in the cell volume for both structures was observed. Although the cell volume reduction was larger after optimization of the **DHWW** structure, crystallographic density of the **AP** was higher, which can be explained by the relatively large empty channels still present in the optimized **DHWW** structure.

By comparing the lattice energy of optimized crystal structures with that for non-optimized crystal structures (see Table S7), a decrease of the lattice energy was observed for both crystal structures. As may be predicted, reduction of the **DHWW** lattice energy was bigger than that for **AP**, although lattice energy of optimized **AP** structure was still energetically favourable.

The total crystal structure energy and lattice parameters obtained by structure optimization are given in Table S8, and fractional atom coordinates are given in Table S2. The addition of zero-point vibration and thermal correction to the calculated total energy did not alter the energy difference significantly. After this correction the **AP** was still energetically more favourable by  $9.7 \text{ kJ}\cdot\text{mol}^{-1}$ .

**Table S8.** The total energy and lattice parameters obtained after the crystal structure optimization in *CRYSTAL09* for the structures of **AP** and **DHWW**.

	AP	DHWW
Energy, Hartree	-496.7405	-496.7363
E(AP)-E(DHWW), kJ·mol <sup>-1</sup>	-11.0	-
a, Å	8.5616	6.7874
b, Å	11.2490	11.1558
c, Å	7.6354	11.7025
$\beta$ , °	89.26	111.63
d, g·cm <sup>-3</sup>	1.320	1.178
V	735.307	823.687
$\Delta V$ , %	-5.2	-15.8

The total energy of **DHWW** was very similar to that of **AP**, so this theoretical structure could not be considered as completely unrealistic and it may represent a transition structure during the dehydration process.

## References

1. L. Greenspan, *J. Res. Nat. Bur. Stand., Sect. A*, 1977, **81A**, 89-96.
2. K. Veldre, A. Actiņš and A. Kalniņa, Thermal Stability of 3-(2,2,2-trimethylhydrazine)propionate, Solid State Chemistry 2010, Prague, 2010.
3. A. Galwey, *Thermochim. Acta*, 2000, **355**, 181-238.
4. R. Dovesi, V. Saunders, C. Roetti, R. Orlando, C. Zicovich-Wilson, F. Pascale, B. Civalleri, K. Doll, N. Harrison and I. Bush, CRYSTAL09, University of Torino, Torino, Italy, 2009.
5. C. M. Zicovich-Wilson, B. Kirtman, B. Civalleri and A. Ramirez-Solis, *Phys. Chem. Chem. Phys.*, 2010, **12**, 3289-3293.
6. A. Zvirgzdiņš, K. Veldre and A. Actiņš, *Latv. J. Chem.*, 2011, **50**, 64-72.
7. M. J. Frisch, G. W. Trucks, H. B. Schlegel, G. E. Scuseria, M. A. Robb, J. R. Cheeseman, G. Scalmani, V. M. Barone, B.;, G. A. Petersson, H. Nakatsuji, M. Caricato, X. Li, H. P. Hratchian, A. F. Izmaylov, J. Bloino, G. Zheng, J. L. Sonnenberg, M. Hada, M. Ehara, K. Toyota, R. Fukuda, J. Hasegawa, M. Ishida, T. Nakajima, Y. Honda, O. Kitao, H. Nakai, T. Vreven, J. A. J. Montgomery, J. E. Peralta, F. Ogliaro, M. Bearpark, J. J. Heyd, E. Brothers, K. N. Kudin, V. N. Staroverov, R. Kobayashi, J. Normand, K. Raghavachari, A. Rendell, J. C. Burant, S. S. Iyengar, J. Tomasi, M. Cossi, N. Rega, J. M. Millam, M. Klene, J. E. Knox, J. B. Cross, V. Bakken, C. Adamo, J. Jaramillo, R. Gomperts, R. E. Stratmann, O. Yazyev, A. J. Austin, R. Cammi, C. Pomelli, J. W. Ochterski, R. L. Martin, K. Morokuma, V. G. Zakrzewski, G. A. Voth, P. Salvador, J. J. Dannenberg, S. Dapprich, A. D. Daniels, O. Farkas, J. B. Foresman, J. V. Ortiz, J. Cioslowski and D. J. Fox, Gaussian 09, Gaussian Inc., Wallingford, CT, 2009.
8. A. Mishnev, I. Kalvins, L. Aleksejeva and A. Lebedev, Structure of Mildronate, its Pharmaceutical Salts and Cocrystals, XXII Congress and General Assembly of the International Union of Crystallography, Madrid, Spain, 2011.
9. A. Gavezzotti, *New J. Chem.*, 2011, **35**, 1360-1368.